



# The nanocrystalline and high density dislocation-Enabled ultrahigh strength and ductility of Al<sub>0.4</sub>Co<sub>0.5</sub>V<sub>0.2</sub>FeNi high entropy alloy

Yuan Li, Zhong Yang, Ping Wang, Hongbo Duan, Wei Yang, Zhijun Ma, Chao Wu, Jianping Li \*

School of Materials and Chemical Engineering, Xi'an Technological University, Xi'an 710021, China



## ARTICLE INFO

### Keywords:

High-entropy alloys  
Duplex-phase  
Severe plastic deformation  
Nanocrystalline  
High density dislocation

## ABSTRACT

The evolution of the microstructure and mechanical properties of a vacuum arc melted non-equiautomic Al<sub>0.4</sub>Co<sub>0.5</sub>V<sub>0.2</sub>FeNi high-entropy alloy (HEA) subjected to severe plastic deformation was investigated experimentally and by simulations. The present work explored duplex HEAs, comprising a face-centered cubic (FCC) matrix and a body-centered cubic (BCC) phase, towards outstanding their mechanical responses. The Al<sub>0.4</sub>Co<sub>0.5</sub>V<sub>0.2</sub>FeNi alloys had a duplex structure, i.e., with dispersed B2-phase islands (with sizes of dozens of microns) in several hundred micron-, even millimeter-sized FCC grains. The mechanical properties of this HEA were strongly deformation dependent, i.e., when deformation increased from 30 % up to 60 %, the yield strength and ultimate strength tensile increased from ~0.9 GPa and 1.0 GPa to ~1.2 GPa and 1.3 GPa, respectively. During tensile deformation, initial fractures occurred in the FCC phase located close to the interface between the FCC and BCC phases. With an increase of deformation, the fracture degree in the FCC phase got larger, and fractures also appeared in the BCC phase. Combined with the geometric dislocation density calculation results from an electron backscatter diffraction (EBSD) analysis, it can be seen that the dislocation density near the phase interface of FCC was higher, making it more likely to produce defects.

## 1. Introduction

In recent years, novel alloys named high entropy alloys (HEAs), which are based on mixing multiple elements in high concentrations and are quite different from the conventional metal materials mainly developed with one principal element, have attracted much attention [1–5]. In early studies, the design concept of HEAs was aimed at obtaining single-phase solid solutions. Such well-designed face-centered cubic (FCC) HEAs exhibit excellent damage tolerance and good ductility, however, the insufficient strength of single-FCC HEAs restrict their structural applications [6–8].

To optimize the strength-ductility combination, extensive research has focused on the activation of various strengthening mechanisms such as solid solution hardening, transformation-induced plasticity (TRIP), microband-induced plasticity (MBIP), twinning induced plasticity (TWIP), and second-phase strengthening [9–13]. The fundamental strengthening criterion related to the deformation modes include dislocation slips and deformation twinning in FCC HEAs. Severe plastic deformation induced via rolling, high-strain-rate deformation, or high pressure torsion is known to cause extensive twinning in FCC-based

HEAs, presumably triggered by the higher internal stresses created during deformation [14–16]. Zhang et al., regulated the microstructure and mechanical property of an NiCoCr-based alloy through hot rolling and achieved a good match of strength and plasticity [17]. Hyeonseok designed a novel Fe-based medium-entropy alloy with a chemical composition of Fe<sub>60</sub>Co<sub>25</sub>Ni<sub>10</sub>Mo<sub>5</sub>. The alloy was manufactured via a simple conventional fabrication route involving casting, homogenization, rolling, and short aging heat treatment, which generated a microstructure consisting of lath martensite, dense nanoprecipitates, and a reverted FCC phase [18].

Additionally, Lu et al., [19] proposed eutectic HEA, and successfully developed the AlCoCrFeNi<sub>21</sub> alloy, which was prepared with an alternating fine soft L12 and hard B2 lamellar structure. Because of the soft L12 and hard B2 lamellar structure, these alloys exhibited excellent mechanical properties. AlCoFeNiC<sub>0.08</sub> HEAs consist of single B2 and FCC phases, and exhibit excellent comprehensive mechanical properties [20].

AlCoVFeNi alloy has been reported by many scholars as a new duplex high-entropy alloy [21]. Ye et al., fabricated the Al<sub>0.25</sub>CoVFeNi HEA, which exhibits a dual-phase microstructure consisting of FCC and BCC

\* Corresponding author.

E-mail address: [jpli\\_0416@163.com](mailto:jpli_0416@163.com) (J. Li).

phases [22]. Vanadium is an optimal element for strengthening FCC high-entropy alloys. However, V easily forms intermetallic compounds and reducing the V content can effectively avoid the generation of intermetallic phases. Hence, we designed the non-equiautomic Al<sub>0.4</sub>Co<sub>0.5</sub>V<sub>0.2</sub>FeNi HEA and studied the cast microstructure and mechanical properties [23]. In this work, we systematically study the microstructure evolution and mechanical properties of Al<sub>0.4</sub>Co<sub>0.5</sub>V<sub>0.2</sub>FeNi HEAs by inducing various strengthening mechanisms that can be activated.

## 2. Materials and methods

### 2.1. Sample preparation

The Al<sub>0.4</sub>Co<sub>0.5</sub>V<sub>0.2</sub>FeNi HEA was obtained by arc melting in a water-cooled copper mold and high-purity argon protective atmosphere at least five times to enhance the chemical homogeneity. Ingots with dimensions of 80 × 25 × 10 mm<sup>3</sup> were directly cold rolled (CR) at 25 °C to sheets in multiple passes with a thickness reduction of ~30 % (CR-30 %), 40 % (CR-40 %), 50 % (CR-50 %), and 60 % (CR-60 %) to retain a suitable density of dislocations in the full matrix, particularly making the blocky B2 phase turn into a lath-shaped one.

### 2.2. Microstructural characterization and tensile tests

The phases in the HEAs were identified by a Bruker D8 X-ray diffraction (XRD) machine with Cu K $\alpha$  radiation, which scanned between 20° and 100° 2 $\theta$  at a scanning rate of 5°/min in the two-dimension mode. The collected data were then analyzed using the Jade V6.5 software and compared to known powder diffraction files (PDFs) for the phases. The microstructures were characterized using a VEGA IIXMU scanning electron microscope (SEM), an optical microscope (OM), and a JEOL JEM-2010 transmission electron microscope (TEM). The chemical compositions were analyzed by energy dispersive spectroscopy (EDS). The volume fractions of the phases in the alloys were measured using the Image-Pro software. The specimens used for the TEM analysis were prepared by a precision ion polishing system. For the ion polishing, the specimens were prepared in a disk shape with a 3 mm diameter and their thicknesses were reduced by grinding to 50–60  $\mu$ m. Tensile tests to failure were carried out at room temperature and an initial strain rate of 1 × 10<sup>-3</sup> s<sup>-1</sup> using an LFM-125 electromechanical machine.

### 2.3. Molecular dynamics simulations

Molecular dynamics (MD) simulations were performed to study the tensile deformation mechanisms in the AlCoVFeNi HEA. The LAMMPS code was used to realize the MD simulation, and the Open Visualization Tool (OVITO) was used to visualize the evolution process of the atomic structure [24–26]. Atomic configurations and dislocation characteristics are presented by OVITO using the dislocation extraction algorithm (DXA). The Atomsk software was used to establish the polycrystalline model. The main steps of which are as follows:

- (1) Calculate the equilibrium lattice constant. Facilitate rapid convergence in energy minimization.
- (2) Establish the model. First, a biphasic model consisting of FCC + BCC phases was established, and then a polycrystalline polyphase model was established with the Voronoi algorithm given the node distribution position.
- (3) The model reached steady state. The energy minimization and relaxation of the atomic model were simulated by setting the potential function to make the model reach a stable state.

In this paper, the embedded atom method (EAM) potential function is used to describe the MD simulation of HEAs [27,28]. The specific expression is as follows:

$$E = F_a \sum_{i \neq j} \rho_i(R_{ij}) + \frac{1}{2} \sum_{i \neq j} \varphi_{x,y}(R_{ij})$$

where  $E$  is the total energy,  $F$  is the embedding energy,  $\varphi$  was the short-range pair potential energy,  $\rho$  is the electron density, and  $x$  and  $y$  are the element types. The reliability of this potential function has been demonstrated in many studies [29,30].

The preparation process of the material was no longer fitted here, because in the process of high-temperature heating, the atomic kinetic energy increased and the range of motion increased, resulting in the breakdown of the ordered FCC and BCC states of the atoms. After cooling, a stable polycrystalline polyphase model could not be obtained, and as the cooled model was highly correlated with the cooling rate, the preparation process was no longer simulated in the polycrystalline model [27–29].

## 3. Results

### 3.1. Microstructural evolution with processing steps

The XRD results of the Al<sub>0.4</sub>Co<sub>0.5</sub>V<sub>0.2</sub>FeNi alloys in different CR states are presented in Fig. 1(a). All samples were mainly composed of FCC and BCC phases. It is worth noting that as the deformation increases, the (111) and (220) diffraction peak of the FCC phase is higher than the (111) diffraction peak of the BCC phase. The higher peak intensity implies that alloys are FCC-dominated structures. The CR samples had a duplex structure, showing dispersed B2-phase islands (sizes of dozens of microns) in several hundred micron-, even millimeter-sized, FCC grains. Figs. 1(b) and 2(c) respectively show the microstructure and EDS map of the alloy after CR30% reduction. The CR process results in a refined microstructure of the FCC matrix, featured by randomly deformed grains. The deformation introduced noticeable changes to the microstructure of the CR50% and CR60% alloys, compared with the CR30% alloy. With an increase of deformation, the microstructure of the CR sample along the rolling direction (RD) view was characterized by a lath-shaped BCC phase (Fig. 1(b), 1(d), 1(f), and 1(h)). The CR-60 % sample shows a mixture of FCC (~84.3 %) and BCC phases (~15.7 %); see Fig. 1(j). The EDS map results shown in Fig. 1(c), 1(e), 1(g), and 1(i) reveal that the FCC phase is rich in V, Fe, and Co, while the BCC phase is rich in Al and Ni. The change of FCC morphology was indicative of its good plastic deformability, which did not crack during CR. Moreover, the nanohardness of the B2 phase was ~8.6 GPa, while that of the FCC grains was ~6.5 GPa (Fig. 1(l)). In this regard, the strength discrepancy between the FCC matrix and BCC phase would cause strain incompatibility so as to trigger the generation of massive geometrically necessary dislocations (GNDs) in the around the hard B2 phase to accommodate the strain gradient (see Fig. 1(k)).

Fig. 2 shows a polar diagram (PF) and inverse polar diagram (IPF) of the CR-60 % sample, where X0 represents RD and Y0 represents ND, which helped us to understand the deformation texture variation law in the rolling process. It can be seen that {111}<sub>FCC</sub> and {110}<sub>BCC</sub> had an obvious K-S orientation relationship. When the rolling amount was 60 %, the FCC and BCC phases showed different texture distribution characteristics, where the FCC alloy showed a {111} // TD, {110} {112}, and {110} {230} random distribution texture. The BCC alloy formed an obvious {111} // RD, {100} // RD, {100} // TD, {100} // ND, and {110} {112} texture. It was further revealed that there were more slip systems and slip planes in the FCC phase during CR deformation. BCC had an obvious preferential deformation along the {110}, {100}, {100}, and {110} directions. After CR, the larger FCC crystals in the original as-cast alloy deformed to a certain extent or even broke their grains, which made the internal grains of the HEAs extend and deform along the RD, leading to different degrees of grain boundary fractures. The grain deformation of the Al<sub>0.4</sub>Co<sub>0.5</sub>V<sub>0.2</sub>FeNi HEA was larger when the deformation amount increased from 30 % to 60 %. In the process of plastic

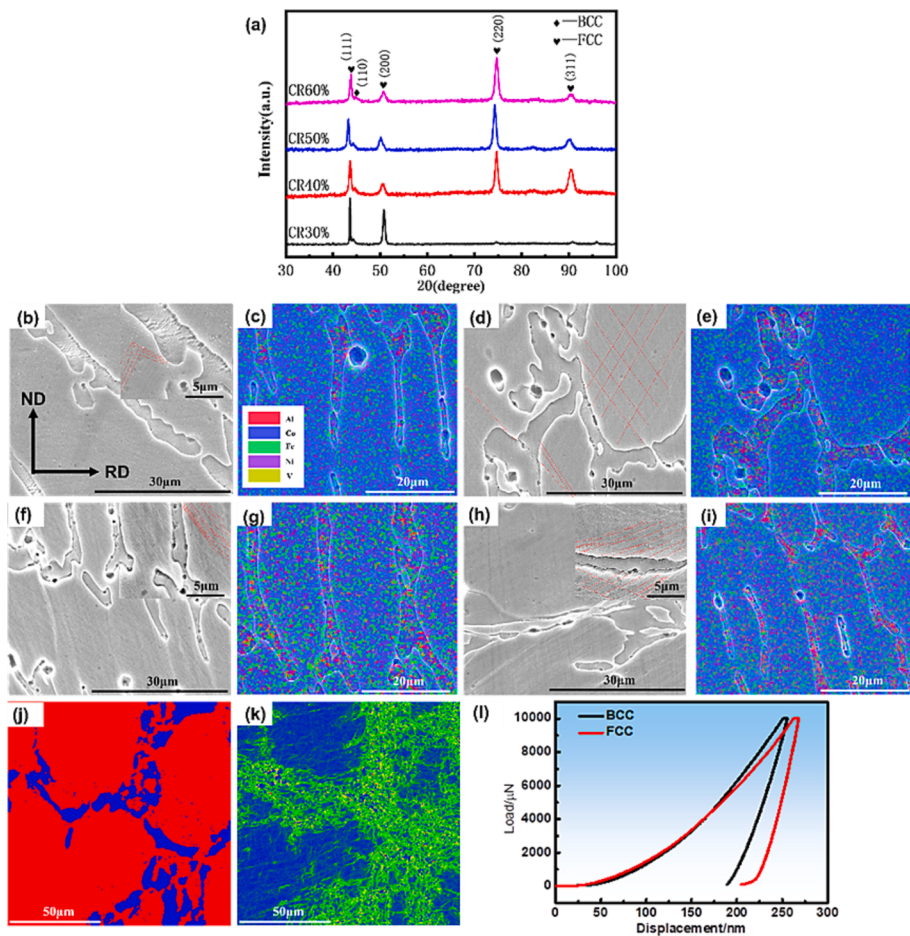


**Fig. 1.** XRD patterns of the  $\text{Al}_{0.4}\text{Co}_{0.5}\text{V}_{0.2}\text{FeNi}$  HEAs and microstructural features of the HEAs after CR. (a) XRD patterns of the  $\text{Al}_{0.4}\text{Co}_{0.5}\text{V}_{0.2}\text{FeNi}$  HEAs in different CR states. (b) SEM micrograph and (c) EDS map of the CR-30 % sample. (d) SEM micrograph and (e) EDS map of the CR-40 % sample. (f) SEM micrograph and (g) EDS map of the CR-50 % sample. (h) SEM micrograph and (i) EDS map of the CR-60 % sample (j) EBSD maps showing blocky B2-phase islands surrounded by an FCC matrix. (k) KAM images (corresponding to Fig. 2(j)), showing abundant residual dislocations in the CR-60 % sample. (l) Load-displacement curves of the CR-60 % sample.

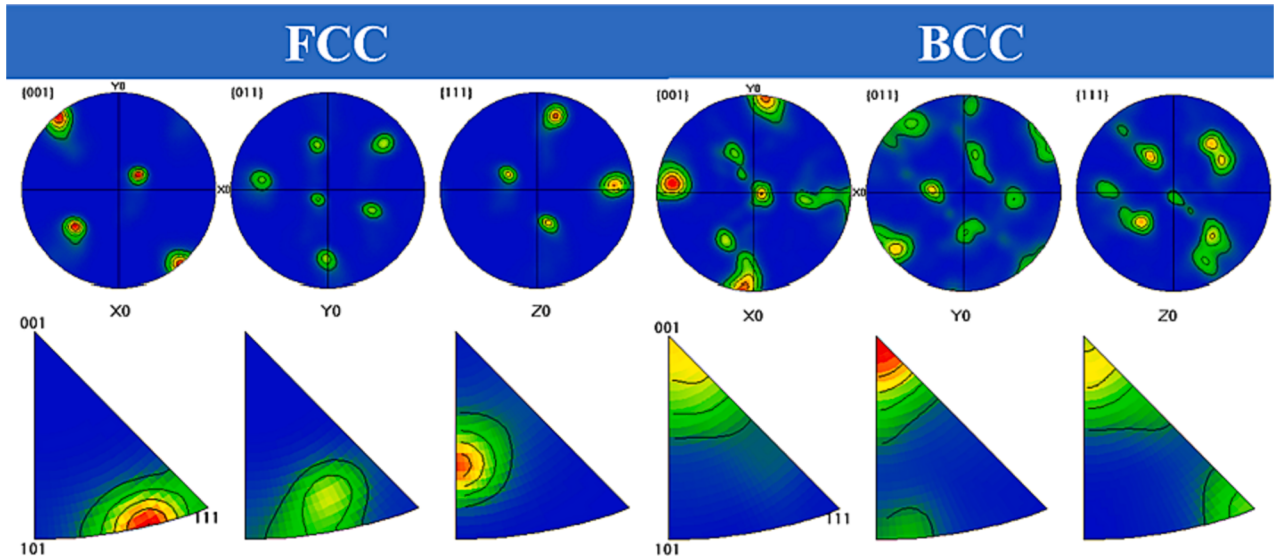


**Fig. 2.** PF and IPF diagrams of the CR-60% sample.

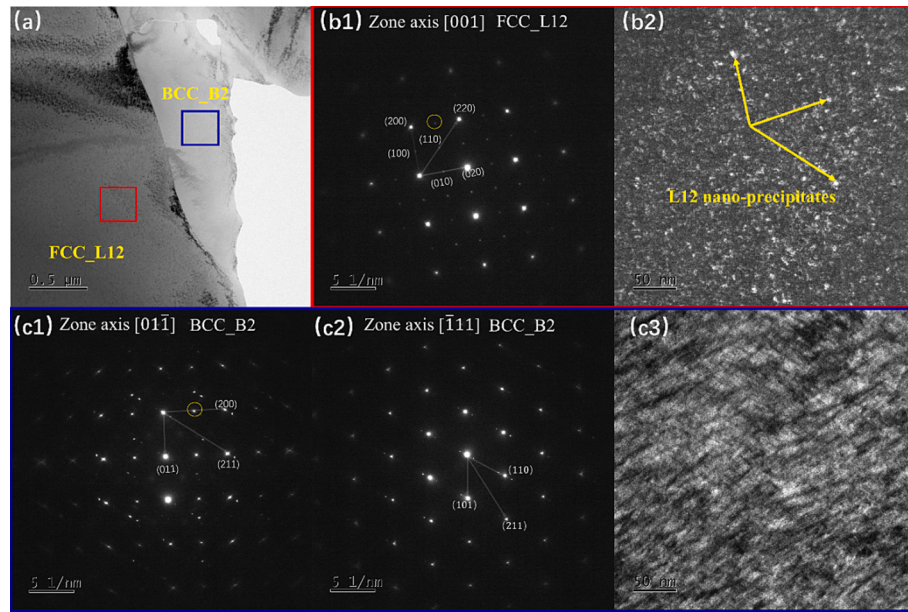


**Fig. 3.** Microstructure of the  $\text{Al}_{0.4}\text{Co}_{0.5}\text{V}_{0.2}\text{FeNi}$  as-cast alloy. (a) Bright field (BF) image of the  $\text{Al}_{0.4}\text{Co}_{0.5}\text{V}_{0.2}\text{FeNi}$  as-cast alloy. (b1) Selected area electron diffraction (SEAD) pattern of the FCC. (b2) Dark field (DF) image of FCC in the HEA from (a). (c1), (c2) The SEAD pattern of the BCC. (c3) DF image of the BCC in the HEA from (a).

deformation, the dislocation defects in the grain also slipped, resulting in a stripped shape and an uneven distribution of the structure.

The TEM image and selected-area electron diffraction patterns of the  $\text{Al}_{0.4}\text{Co}_{0.5}\text{V}_{0.2}\text{FeNi}$  as-cast alloy are shown in Fig. 3. There are the weak superlattice spots in the selected area electron diffraction patterns (SADPs), which means that the FCC phase and BCC phase are both ordered, with L12 and B2 structures, respectively. The analysis and characterization of diffraction spots are consistent with those reported in other studies [31,32]. The red region exhibits additional super-lattice reflections in the [001] FCC zone axis as shown in the inset in Fig. 3(b1), which indicates the presence of a high-density density-ordered L12 within the FCC matrix existing in the FCC (Fig. 3(b3)). In the blue region, the SADPs from the [01 $\bar{1}$ ] and [ $\bar{1}$  11] zone axes indicate that only the BCC-B2 phase exists, as shown in Fig. 3(c1) and (c2). Fig. 3(c3) presents the lamellar structure of the BCC\_B2 phase, which is quite common in other BCC\_B2 phases [33].

In order to investigate further the microstructure differences of the CR samples, TEM experiments were conducted, and the images taken at the transverse direction (TD)-RD plane are displayed in Fig. 4. Fig. 4(a) shows a series of BF images of the CR-30 % sample. The inset shows an SEAD pattern of the FCC matrix. Microscale deformation twins (DTs) and deformation bands (DBs) are observed in stretched FCC phases, as shown in Fig. 4(a). High-density dislocations appear in the FCC phases and around the DBs, confirming that the grain DBs play a positive role in strengthening the alloy. At the CR40% reduction, the high-density planar slip of dislocations in the FCC planes is a dominant feature, as shown in Fig. 4(b). Observation at high magnification of the area marked with a red square in Fig. 4(b) reveals that high-density stack faults (SFs) are generated in the L12 phase. The deformation characteristics of L12 phase are consistent with those reported in other studies [34,35]. Nanoprecipitates can impede the dislocation motion seen in Fig. 4(b). By increasing the rolling extent to 50 %, SFs are found between the dislocations paths and DBs, which further accumulate the plastic deformation and suppress the expansion of dislocation paths, as seen in Fig. 4(c). Dislocation cells appeared in the red region where a large number of nanometer precipitates had been generated, and a high-density slip zone appeared along with dislocation cells. The formation of dislocation cells and the high-density slip zone was due to the interaction of dislocation motion under CR. This feature indicates that local

inhomogeneous plastic deformation occurs during heavy CR. Fig. 4(d) shows a series of BF-STEM images of the CR-60 % sample. A large number of high-density nanocrystals appeared in the FCC matrix. The diffraction results show the presence of polycrystalline rings, indicating that the local plastic deformation of the matrix under this deformation amount caused severe grain breakage. High-density dislocations and DTs could still be found in different views of the field. The images recorded from one of the twin variants reveal multiple DTs with varying thicknesses from 30 nm to 60 nm.

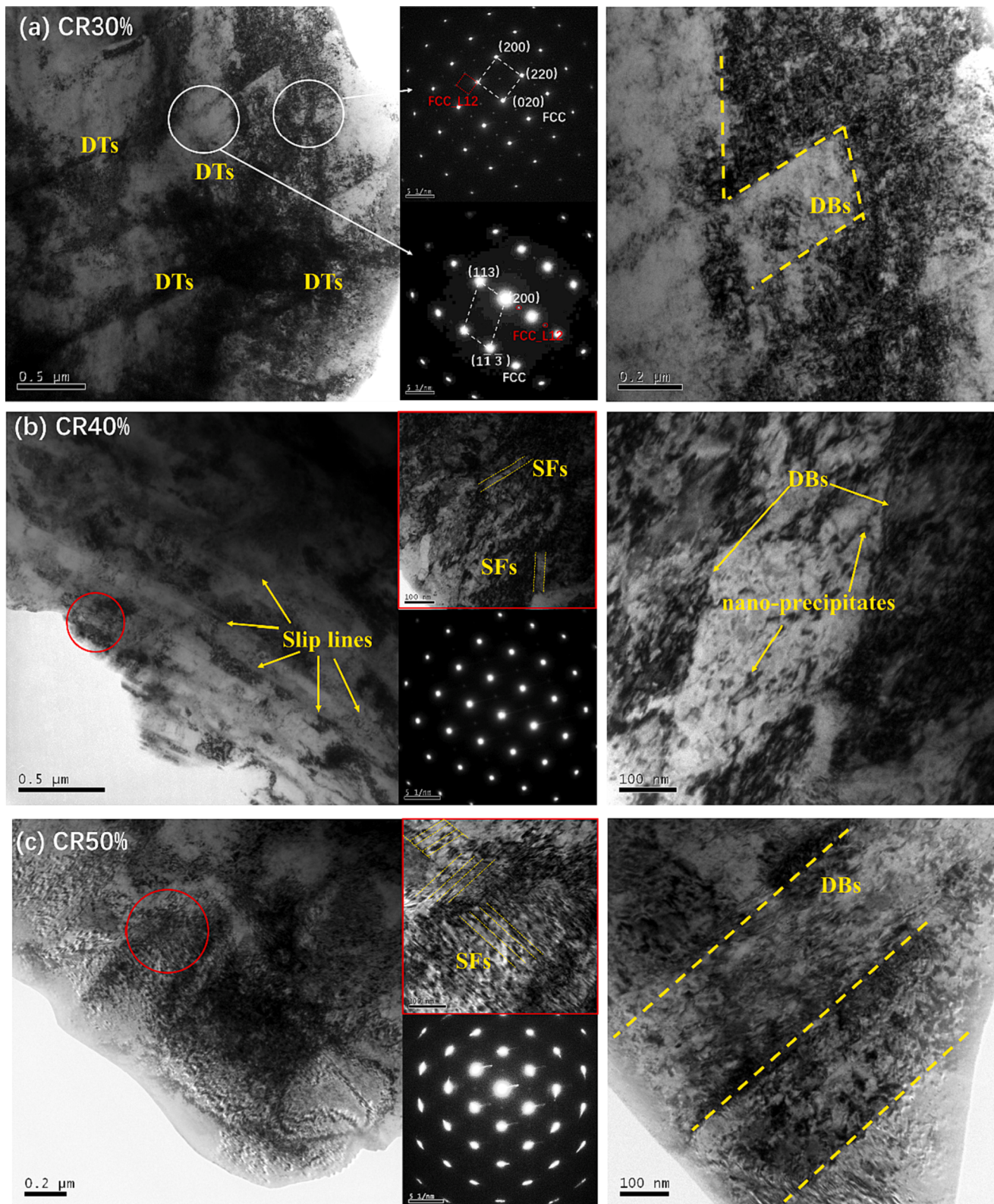
### 3.2. Mechanical properties

Fig. 5 shows the tension test results for the CR samples at room temperature. According to the results, with an increase of deformation, the tensile strength and yield strength of the materials increased, while the elongation decreased slightly (see Table 1). As the deformation increased from 30 % to 60 %, the yield strength and ultimate strength tensile increased from  $\sim 0.9$  GPa and  $\sim 1.0$  GPa to  $\sim 1.2$  GPa and  $\sim 1.3$  GPa, respectively. The as-cast sample had mechanical properties with a yield strength of 372 MPa, tensile strength of 722 MPa, and an elongation of 38.3 %. After rolling at 60 %, the sample showed a high yield strength of 1195 MPa and an ultimate tensile strength of 1334 MP. Compared with the cast state, the ultimate tensile strength of CR60% increased by nearly 85 %. The outstanding strength properties of CR60% are attributed to the volume fraction of dislocations, which play an important role in strengthening by reducing plasticity.

## 4. Discussion

### 4.1. Nanocrystal behavior in the present duplex CR-60 %

Fig. 6 shows the TEM morphologies of the matrix and nanocrystals of the 60 % rolled alloy. Fig. 6(a) displays the overall morphology of the matrix. Long strips of nanocrystalline grains appear in the matrix. The matrix is marked in red and the nanocrystalline grains are marked in blue. Fast Fourier transform (FFT) images of the matrix and nanocrystalline grains showed that the matrix had a typical FCC-phase structure, and the nanocrystalline grains had obvious directivity and the diffraction characteristics of FCC polycrystals (twins). According to a



**Fig. 4.** Microstructure of the  $\text{Al}_{0.4}\text{Co}_{0.5}\text{V}_{0.2}\text{FeNi}$  alloy after CR treatment.

high-angle annular dark field scanning (HADF) characterization analysis, there is almost no difference in the composition between the matrix and nanocrystalline phase, which proves that there was no amplitude modulation decomposition; instead, the formation of the nanocrystalline phase was caused by deformation in the rolling process.

**Fig. 7** shows the formation mechanism of the nanocrystals. It can be seen that in the deformation process of the matrix, excess semi-atomic planes were generated in the matrix to form a large number of edge dislocations, resulting in a large number of dislocations plugging and passing through the nanograins. Shen et al., [36] found in a study of pure

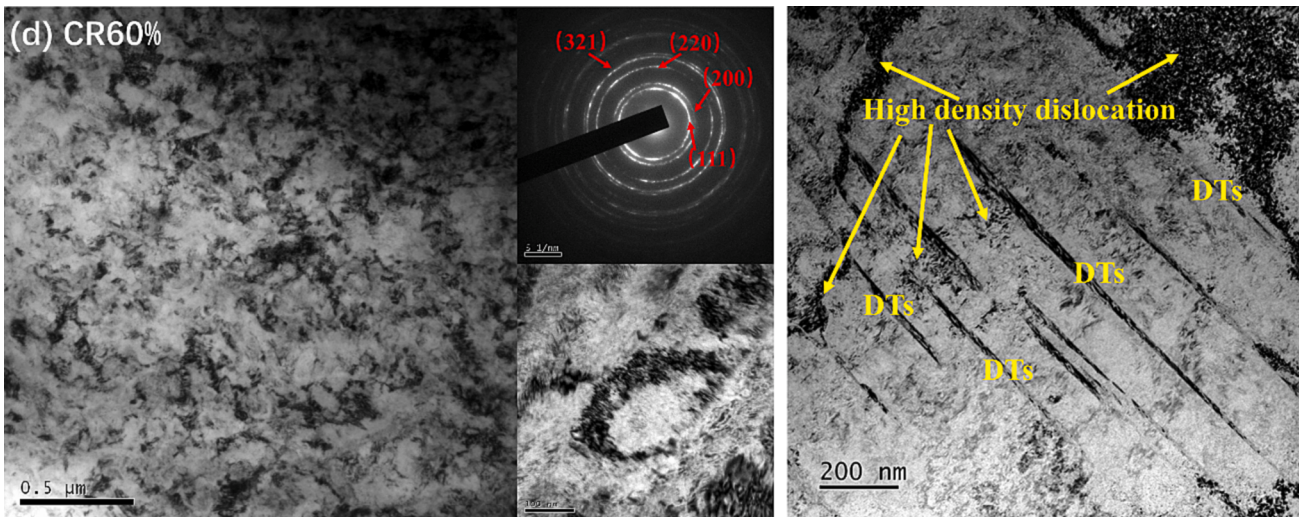


Fig. 4. (continued).

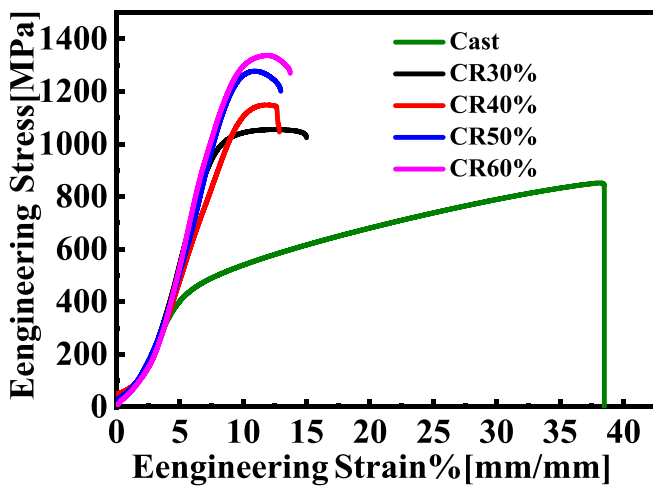
Fig. 5. Mechanical responses of the  $\text{Al}_{0.4}\text{Co}_{0.5}\text{V}_{0.2}\text{FeNi}$  alloy tested at 298 K.

Table 1

Ultimate Tensile Strength (UTS), Yield Strength (YS), and Elongation (E) to Failure of the HEA samples.

	UTS (MPa)	YS (MPa)	E (%)
CR30%	1051	976	15.2
CR40%	1149	1076	12.8
CR50%	1276	1164	12.7
CR60%	1334	1195	13.6
Cast	722	372	38.3

Cu samples containing high density nanotwins that dislocations mainly moved along the  $\{111\}$  slip inclined to and towards the nanocrystal boundary during plastic deformation, and eventually accumulated near the nanocrystal boundary due to the blocking effect of the boundary. With an increase of deformation, the leading dislocation of the plug product group reacted with the twin boundary, crossing it into the next twin lamella driven by stress concentration; such behavior is similar to the phenomenon found in this study. In the deformation process, local regions formed a nanoscale plastic zone and store part of the shear strain energy; this caused the dislocations to clog further and tangle to form subcrystals, which will be transformed into large-angle nanometer grains [37]. Shabib [38] believed that this grain orientation

recombination effect had an important contribution to the matching of material strength and toughness.

#### 4.2. Strengthening mechanisms

The excellent performances of the bulk alloys synthesized by CR were associated with the combined effect of several strengthening mechanisms: solid solution strengthening by component elements, grain boundary strengthening by ultrafine grains, dislocation strengthening by high density defects, and Orowan strengthening by precipitated phases. The stretched yield strength of the  $\text{Al}_{0.4}\text{Co}_{0.5}\text{V}_{0.2}\text{FeNi}$  HEA can be expressed as follows [39]:

$$R_{p0.2} = \Delta\sigma_{ss} + \Delta\sigma_{gb} + \Delta\sigma_{or} + \Delta\sigma_{dis}$$

where  $\Delta\sigma_{ss}$ ,  $\Delta\sigma_{gb}$ ,  $\Delta\sigma_{or}$ , and  $\Delta\sigma_{dis}$  are the strengthening contributions of the solid solution, grain boundary, Orowan, and dislocation strengthening, respectively.

The relatively high density of initial dislocations in CR is attributed to severe plastic deformation. The value of  $\Delta\sigma_{dis}$  can be expressed as [40]:

$$\Delta\sigma_{dis} = M\alpha G b p^{1/2}$$

where  $M$  is the Taylor factor,  $\alpha$  is a constant (where FCC is generally 0.2 and BCC is 0.38),  $G$  is the shear modulus,  $b$  is the Bergdahl vector, and  $p$  is the dislocation density. The shear modulus is calculated with the Material Studio software based on first principles. The most stable structure is determined by calculating the phase stability of FCC and BCC phases (see Fig. 8).

The average value of the Voigt approximation ( $G_V$ ) and Reuss approximation ( $G_R$ ) for the shear modulus  $G$  are given, respectively, as:

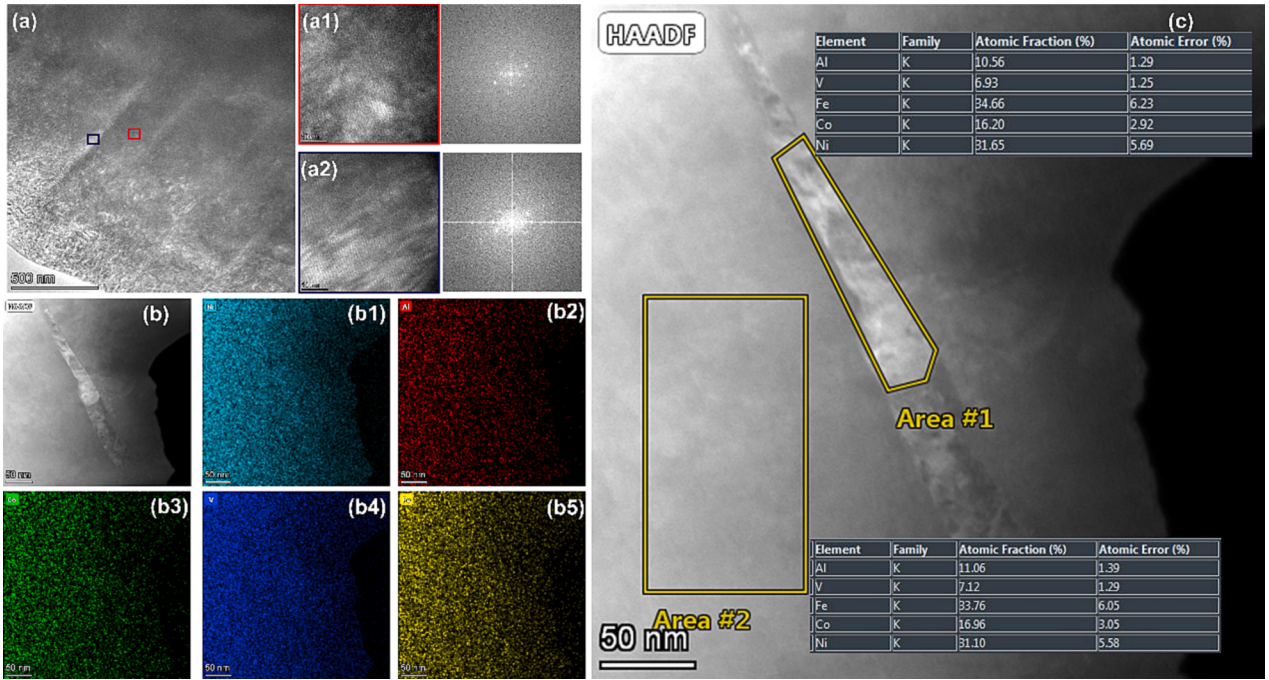
$$G_R = \frac{5(C_{11} - C_{12})C_{44}}{4C_{44} + 3(C_{11} - C_{12})}$$

$$G_V = \frac{C_{11} - C_{12} + 3C_{44}}{5}$$

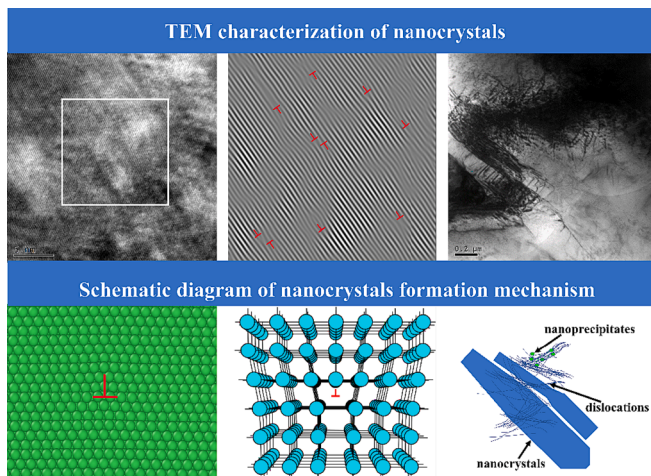
$$G = \frac{G_V + G_R}{2}$$

Table 2 shows Elastic Constant ( $C_{ij}$ ) of the  $\text{Al}_{0.4}\text{Co}_{0.5}\text{V}_{0.2}\text{FeNi}$  HEAs. By calculation, the shear modulus of the BCC phase is 252.49 GPa and the shear modulus of the FCC phase is 138.22 GPa.

A microstructure with a hierarchical grain size, an inhomogeneous distribution of dislocations, multiple phases, and/or precipitates could



**Fig. 6.** HRTEM characterization of the CR-60% alloy. (a) HRTEM image exhibiting nanocrystals embedded inside the matrix. (a1)–(a2) Filtered and inverted FFT patterns of the matrix and nanocrystals phases, respectively. (b) Element distributions of the matrix and nanocrystals regions determined in the HAADF analysis.



**Fig. 7.** The nanocrystalline formation mechanism.

be a source of a high density of GNDs. The density of dislocations was calculated based on electron backscatter diffraction (EBSD) data, which is expressed as:

$$\rho = \frac{2\theta_{KAM}}{Xb}$$

where  $\theta_{KAM}$  is the kernel average misorientation (KAM) retrieved from EBSD data ( $\theta_{KAM,FCC} = 1.85$ ,  $\theta_{KAM,BCC} = 2.62$ ) shown in Fig. 9(b) and (e).  $X$  is the kernel size (600 nm), which is equal to twice the step size used in EBSD acquisition.  $b$  is the Burgers vector ( $b_{FCC} = 0.254$  nm,  $b_{BCC} = 0.249$  nm), which can be obtained by XRD. By calculation, the dislocation density of FCC is  $2.43 \times 10^{16} \text{ m}^{-2}$  and that of BCC is  $3.51 \times 10^{16} \text{ m}^{-2}$ .

The FCC Taylor factor is 3.35 and the BCC Taylor factor is 2.58, which were calculated using the data shown in Fig. 9(c) and (f). The calculated FCC contribution value is about 464.52 MPa, and the BCC contribution value is about 246.12 MPa. Therefore, the yield strength contributed by dislocation strengthening is about 710 MPa. The actual yield strength of the material is 1195 MPa. Therefore, dislocation strengthening is the main strengthening mechanism of this dual-phase

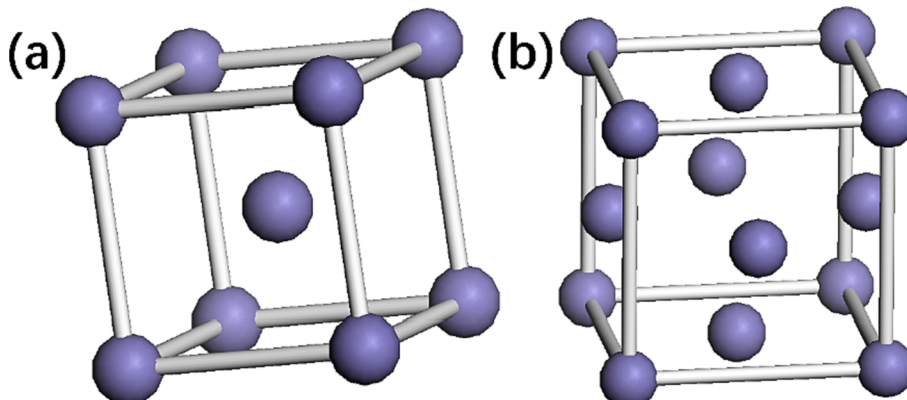


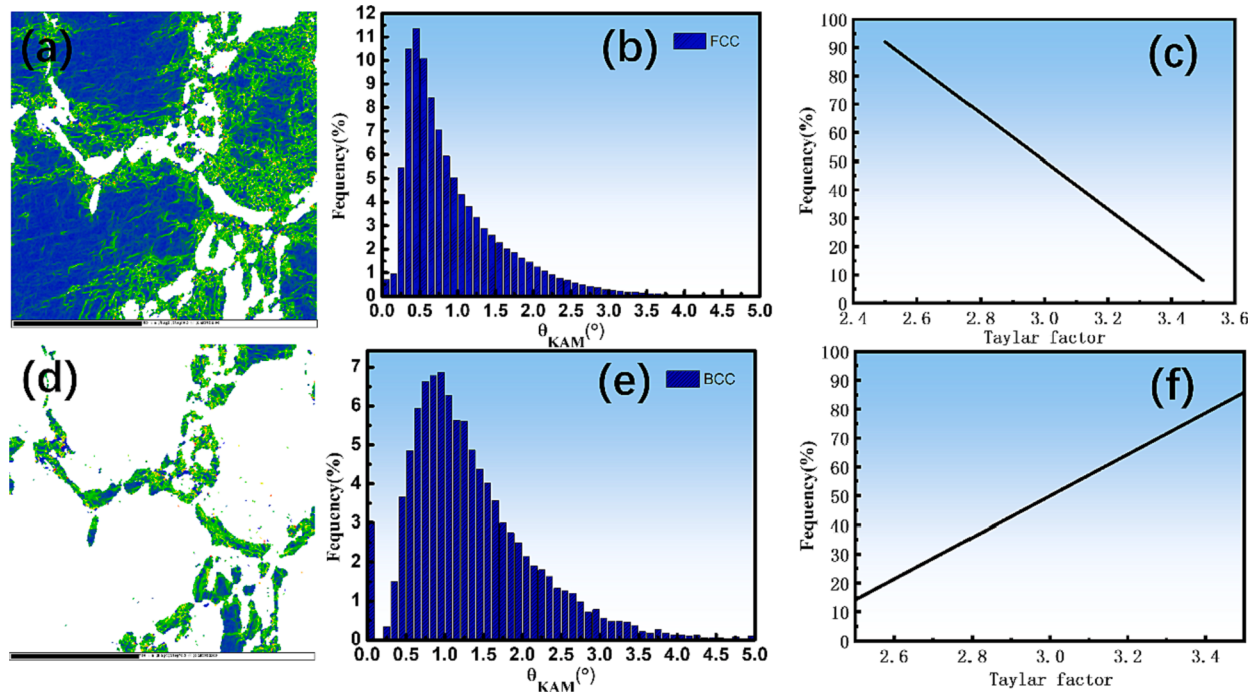
**Fig. 8.** BCC and FCC structure models of the  $\text{Al}_{0.4}\text{Co}_{0.5}\text{V}_{0.2}\text{FeNi}$  HEAs: (a) BCC and (b) FCC.

**Table 2**Elastic Constant ( $C_{ij}$ ) of the  $\text{Al}_{0.4}\text{Co}_{0.5}\text{V}_{0.2}\text{FeNi}$  HEAs.

$C_{11}$	$C_{12}$	$C_{44}$
BCC	FCC	BCC
-67.26285	270.09225	164.67265

$C_{11}$	$C_{12}$	$C_{44}$
FCC	BCC	FCC
55.57085	108.95450	163.78090

**Fig. 9.** (a) KAM images of the FCC phases, showing abundant residual dislocations. (b)  $\theta_{\text{KAM}}$  of the FCC phases. (c) Taylor factor of the FCC phases. (d) KAM images of the BCC phases, showing abundant residual dislocations (e)  $\theta_{\text{KAM}}$  of the BCC phases. (f) Taylor factor of the BCC phases.

HEA.

#### 4.3. Tensile deformation mechanisms

In order to study the microstructure evolution of the  $\text{Al}_{0.4}\text{Co}_{0.5}\text{V}_{0.2}\text{FeNi}$  HEA under tensile loads at room temperature, the tensile deformation process of the HEA at (298 K) was simulated by MD. Lamps were used to construct a  $20 \text{ nm} \times 18 \text{ nm} \times 21 \text{ nm}$   $\text{Al}_{0.4}\text{Co}_{0.5}\text{V}_{0.2}\text{FeNi}$  polyphase polycrystal model. Based on polyhedral template matching (PTM), the recognized FCC atoms, BCC atoms, hexagonal close packed (HCP) atoms, and hexagonal diamond atoms are shown in Fig. 10 in green, blue, red, and orange, respectively. The total number of simulated atoms was 643,819, and the MD simulation of tensile strength at room temperature was carried out.

Fig. 10(d)–(f) show the simulated microstructure morphology evolution process of  $\text{Al}_{0.4}\text{Co}_{0.5}\text{V}_{0.2}\text{FeNi}$  obtained by the MD simulation. It can be seen that initial fractures occurred in the FCC phase, close to the interface between the FCC and BCC phases. With an increase of deformation, the fracture degree in the FCC phase gets larger, and fractures also appear in the BCC phase. Fig. 10(g) shows the dislocation distribution in the tensile process of the  $\text{Al}_{0.4}\text{Co}_{0.5}\text{V}_{0.2}\text{FeNi}$  HEA. It can be seen that the dislocations in the deformation process are mainly  $1/6 \langle 112 \rangle$  Shockley partial dislocations, with a small number of  $1/6 \langle 110 \rangle$ ,  $1/2 \langle 110 \rangle$ , and  $1/3 \langle 112 \rangle$ . Among them,  $1/6 \langle 112 \rangle$ ,  $1/2 \langle 110 \rangle$ , and  $1/6 \langle 110 \rangle$  partial dislocations mainly occur in the FCC phase, and  $1/3 \langle 112 \rangle$  and  $1/6 \langle 112 \rangle$  in BCC. The small number of  $1/6 \langle 112 \rangle$  and  $1/3 \langle 112 \rangle$  in FCC produced  $1/2 \langle 110 \rangle$  total dislocations, and the dislocation reaction is  $a/6 \langle 112 \rangle + a/3 \langle 112 \rangle = a/2 \langle 110 \rangle$  (where  $a$  represents the lattice constant in the alloy). Combined with the geometric dislocation

density calculation results from the EBSD analysis (see Fig. 9(h)), it can be seen that the dislocation density near the phase interface of FCC was higher, so it was more likely to produce defects. Fig. 11 shows the dual-phase interface between FCC and BCC. It can be seen that the dislocation density near the interface of the FCC phase was relatively high, allowing it to form a large number of dislocations easily. The dislocation density of the BCC phase was low. Therefore, in the process of stretching, the stress concentration near the FCC interface was large, easily producing defects. The result is consistent with the simulation results, where defects are generated in the FCC phase, close to the two-phase interface.

#### 5. Conclusions

Non-equiautomatic  $\text{Al}_{0.4}\text{Co}_{0.5}\text{V}_{0.2}\text{FeNi}$  HEA processed by vacuum arc melting and rolling was subjected to severe plastic deformation using the multi-pass technique with a thickness reduction. The evolution of their microstructure and mechanical properties was studied. The tensile deformation of the  $\text{Al}_{0.4}\text{Co}_{0.5}\text{V}_{0.2}\text{FeNi}$  HEA was simulated using MD. After analyzing the experimental data and simulations, the following main conclusions can be made:

1. The  $\text{Al}_{0.4}\text{Co}_{0.5}\text{V}_{0.2}\text{FeNi}$  alloy have a duplex structure, with dispersed B2-phase islands (sizes dozens of micron) in several hundred micron-/millimeter-sized FCC grains. The CR-60 % sample showed a mixture of FCC (~84.3 %) and BCC phases (~15.7 %). The nano-hardness of the B2 phase was  $\sim 8.6 \text{ GPa}$ , while that of the FCC grains is  $\sim 6.5 \text{ GPa}$ . The mechanical properties of the HEA samples were strongly deformation dependent, i.e., when deformation increased from 30 % up to 60 %, the yield strength and ultimate strength

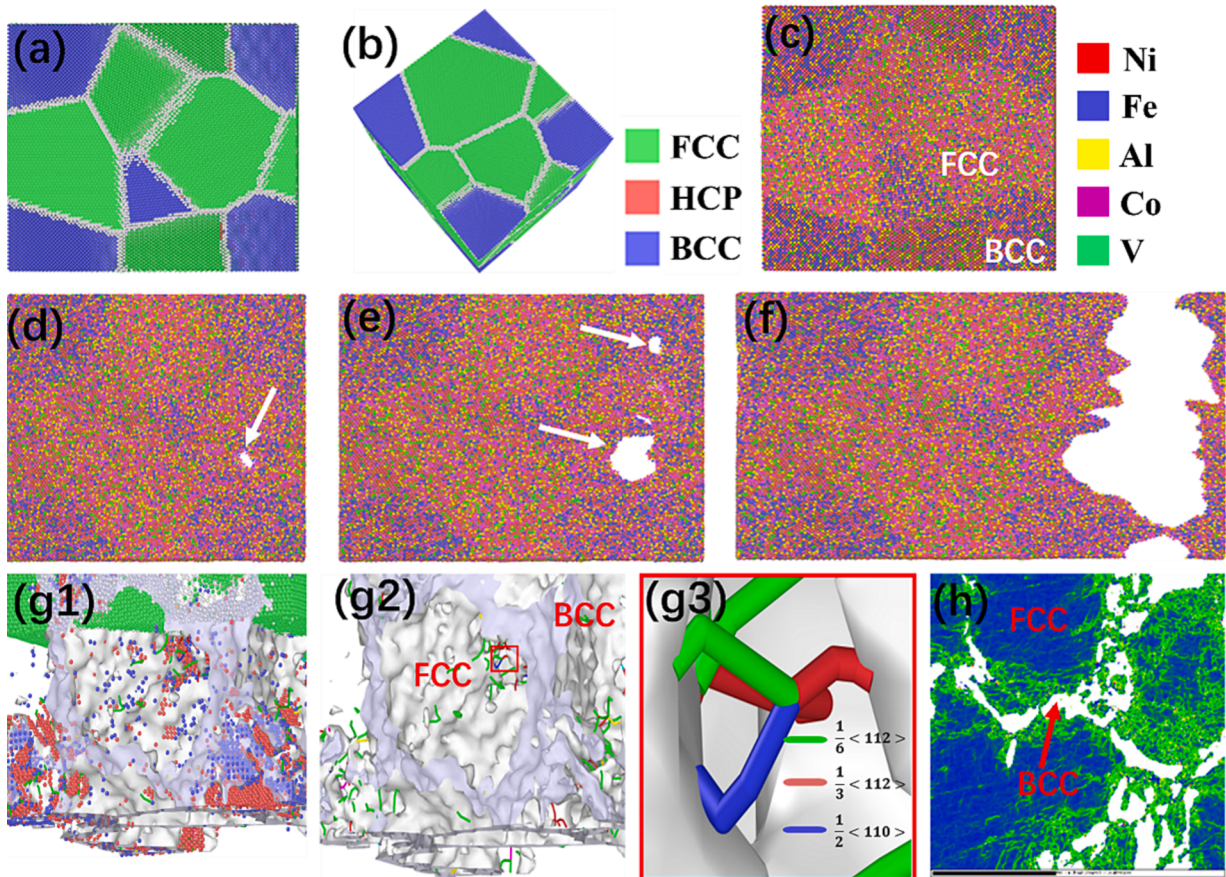


Fig. 10. Tensile evolution of the  $\text{Al}_{0.4}\text{Co}_{0.5}\text{V}_{0.2}\text{FeNi}$  HEAs.

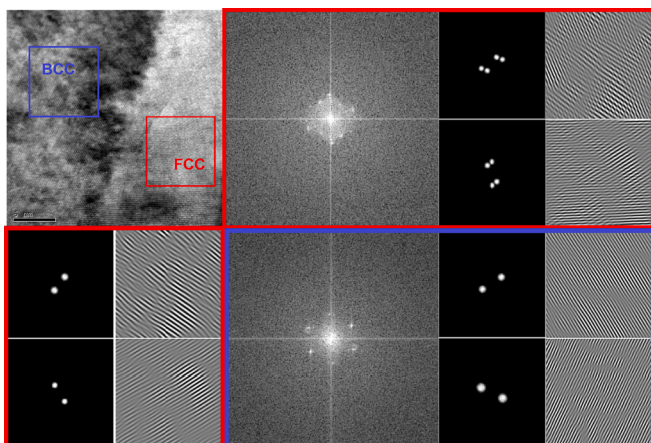


Fig. 11. The interface between the BCC and FCC phases in the  $\text{Al}_{0.4}\text{Co}_{0.5}\text{V}_{0.2}\text{FeNi}$  HEA.

tensile increased from  $\sim 0.9$  GPa and  $1.0$  GPa to  $\sim 1.2$  GPa and  $1.3$  GPa, respectively.

2. After CR, the larger FCC crystals in the original as-cast alloy deformed to a certain extent or even break their grains, which made the internal grains of the HEAs extend and deform along the RD, leading to different degrees of grain boundary fractures. The FCC phase and BCC phase showed different texture distribution characteristics, where the FCC alloy manifested a  $\langle 111 \rangle // \text{TD}$ ,  $\langle 110 \rangle \langle 112 \rangle$ , and  $\langle 110 \rangle \langle 230 \rangle$  random distribution texture. The BCC phase in the alloy formed an obvious  $\langle 111 \rangle // \text{RD}$ ,  $\langle 100 \rangle // \text{RD}$ ,  $\langle 100 \rangle // \text{TD}$ ,  $\langle 100 \rangle // \text{ND}$ , and  $\langle 110 \rangle \langle 112 \rangle$  texture.

3. According to the HADDF characterization analysis, there was almost no difference in the composition between the matrix and nanocrystalline phase, which proved that there was no amplitude modulation decomposition; instead, the formation of the nanocrystalline phase was caused by deformation during the rolling process. In the deformation process, excess semi-atomic planes were generated in the matrix to form a large number of edge dislocations, resulting in a large number of dislocations plugging and passing through the nanograins.

4. The yield strength contributed by dislocation strengthening was about  $710$  MPa. The actual yield strength of the material was  $1,195$  MPa. Dislocation strengthening was the main strengthening mechanism of this dual-phase HEA.

5. During tensile deformation, initial fractures occurred in the FCC phase close to the interface between the FCC and BCC phases. With an increase of deformation, the fracture degree in the FCC phase was larger, and fractures also appeared in the BCC phase. Combined with the geometric dislocation density calculation results from the EBSD analysis, it can be seen that the dislocation density near the phase interface of FCC was higher, making it more likely to produce defects.

#### Declaration of Competing Interest

The authors declare that they have no known competing financial interests or personal relationships that could have appeared to influence the work reported in this paper.

#### Data availability

No data was used for the research described in the article.

## Acknowledgments

This work was supported by National Pre Research General Technology Program of China (No. 50922010401), Excellent Dissertation Cultivation Fund of Xi'an Technological University (No. YB202206), The youth innovation team of engine key component material research, development and application in Shaanxi Universities (No. K20220185).

## References

- [1] J.W. Yeh, S.K. Chen, S.J. Lin, J.Y. Gan, T.S. Chin, T.T. Shun, C.H. Tsau, S.Y. Chang, Nanostructured high-entropy alloys with multiple principal elements: novel alloy design concepts and outcomes, *Adv. Eng. Mater.* 6 (2004) 299–303.
- [2] B. Cantor, Multicomponent and high entropy alloys, *Entropy* 16 (2014) 4749–4768.
- [3] Y.F. Ye, Q. Wang, J. Lu, C.T. Liu, Y. Yang, High-entropy alloy: challenges and prospects, *Mater. Today* 19 (6) (2016) 349–362.
- [4] Y. Zhang, T.T. Zuo, Z. Tang, M.C. Gao, K.A. Dahmen, P.K. Liaw, Z.P. Lu, Microstructures and properties of high-entropy alloys, *Prog. Mater. Sci.* 61 (2014) 1–93.
- [5] D.B. Miracle, O.N. Senkov, A critical review of high entropy alloys and related concepts, *Acta Mater.* 122 (2017) 448–511.
- [6] B. Cantor, I.T.H. Chang, P. Knight, A.J.B. Vincent, Microstructural development in equiatomic multicomponent alloys, *Mater. Sci. Eng. A* 375 (2004) 213–218.
- [7] Z.Z. Li, S.T. Zhao, R.O. Ritchie, M.A. Meyers, Mechanical properties of high-entropy alloys with emphasis on face-centered cubic alloys, *Prog. Mater. Sci.* 102 (2019) 296–345.
- [8] D. Choudhuri, B. Gwalani, S. Gorsse, M. Komarasamy, S.A. Mantri, S.G. Srinivasan, R.S. Mishra, R. Banerjee, Enhancing strength and strain hardenability via de formation twinning in fcc-based high entropy alloys reinforced with intermetallic compounds, *Acta Mater.* 165 (2019) 420–430.
- [9] M. Traversier, P. Mestre-Rinn, N. Peillon, E. Rigal, X. Boulnat, F. Tancré, J. Dhers, A. Fraczkiewicz, Nitrogen-induced hardening in an austenitic CrFeMnNi high-entropy alloy (HEA), *Mater. Sci. Eng. A* 804 (2021), 140725.
- [10] Z. Li, K.G. Pradeep, Y. Deng, D. Raabe, C.C. Tasan, Metastable high-entropy dual-phase alloys overcome the strength-ductility trade-off, *Nature* 534 (7606) (2016) 227–230.
- [11] D. Foley, S. Huang, E. Anber, L. Shanahan, Y. Shen, A. Lang, C. Barr, D. Spearot, L. Lamberson, M. Taheri, Simultaneous twinning and microband formation under dynamic compression in a high entropy alloy with a complex energetic landscape, *Acta Mater.* 200 (2020) 1–11.
- [12] J. Moon, O. Bouaziz, H.S. Kim, Y. Estrin, Twinning engineering of a CoCrFeMnNi high-entropy alloy, *Scripta Mater.* 197 (2021), 113808.
- [13] S.N. Kumararan, S.K. Sahoo, C. Haase, L.A. Barrales-Mora, L.S. Toth, Nano-structuring of a high entropy alloy by severe plastic deformation: experiments and crystal plasticity simulations, *Acta Mater.* 250 (2023), 118814.
- [14] X.D. Xu, P. Liu, Z. Tang, A. Hirata, S.X. Song, T.G. Nieh, P.K. Liaw, C.T. Liu, M. W. Chen, Transmission electron microscopy characterization of dislocation structure in a face-centered cubic high-entropy alloy Al0.1CoCrFeNi, *Acta Mater.* 144 (2018) 107–115.
- [15] B. Schuh, F. Mendez-Martin, B. Völker, E.P. George, H. Clemens, R. Pippan, A. Hohenwarter, Mechanical properties, microstructure and thermal stability of a nanocrystalline CoCrFeMnNi high-entropy alloy after severe plastic deformation, *Acta Mater.* 96 (2015) 258–268.
- [16] S. Mahajan, Critique of mechanisms of formation of deformation, annealing and growth twins: face-centered cubic metals and alloys, *Scripta Mater.* 68 (2) (2013) 95–99.
- [17] D.D. Zhang, J.Y. Zhang, J. Kuang, G. Liu, J. Sun, The B2 phase-driven microstructural heterogeneities and twinning enable ultrahigh cryogenic strength and large ductility in NiCoCr-based medium-entropy alloy, *Acta Mater.* 233 (2022), 117981.
- [18] H. Kwon, P. Sathiyamoorthi, M.K. Gangaraju, A. Zargaran, J. Wang, Y.-U. Heo, S. Harjo, W. Gong, B.-J. Lee, H.S. Kim, High-density nanoprecipitates and phase reversion via maraging enable ultrastrong yet strain-hardenable medium-entropy alloy, *Acta Mater.* 248 (2023), 118810.
- [19] Y. Lu, Y. Dong, S. Guo, L. Jiang, H. Kang, T. Wang, B. Wen, Z. Wang, J. Jie, Z. Cao, H. Ruan, T. Li, A promising new class of high-temperature alloys: eutectic high-entropy alloys, *Sci. Rep.* 4 (2014) 6200.
- [20] J. Peng, Z.-Y. Li, X.-B. Ji, Y.-L. Sun, L.-M. Fu, A.-D. Shan, Decomposition kinetics of carbon-doped FeCoCrNiMn high-entropy alloy at intermediate temperature, *Trans. Nonferrous Met. Soc. China* 30 (7) (2020) 1884–1894.
- [21] H. Duan, Z. Ma, C. Wu, Y. Bai, C.F. Sun, P. Wang, J. Li, Microstructure and mechanical properties of Al0.4Co0.5V0.6FeNi high-entropy alloys processed by homogenization treatment, *Intermetallics* 159 (2023), 107941.
- [22] Z. Ye, C. Li, M. Zheng, X. Zhang, Realizing superior strength-ductility combination in dual-phase AlFeCoNiV high-entropy alloy through composition and microstructure design, *Mater. Res. Lett.* 10 (2021) 736–743.
- [23] Y. Li, Z. Yang, Z. Ma, Y. Bai, C. Wu, J. Li, Effect of element V on the As-cast microstructure and mechanical properties of Al 0.4 Co 0.5 V x FeNi high entropy alloys, *J Alloys Compd.* 911 (2022), 165043.
- [24] S. Plimpton, Fast parallel algorithms for short-range molecular-dynamics, *J. Comput. Phys.* 117 (1995) 1–19.
- [25] A. Stukowski, Visualization and analysis of atomistic simulation data with OVITO—the open visualization tool, *Model Simulat. Mater. Sci. Eng.* 18 (1) (2010), 015012.
- [26] A. Stukowski, Structure identification methods for atomistic simulations of crystalline materials, *Model Simulat. Mater. Sci. Eng.* 20 (4) (2012), 045021.
- [27] M.S. Daw, M.I. Baskes, Embedded-atom method: derivation and application to impurities, surfaces, and other defects in metals, *Phys. Rev. B Condensed Matter* 29 (12) (1984) 6443–6453.
- [28] M.S. Daw, M.I. Baskes, Semiempirical, quantum mechanical calculation of hydrogen embrittlement in metals, *Phys. Rev. Lett.* 50 (17) (1983).
- [29] A. Fourmont, S.L. Gallet, O. Politano, C. Desgranges, F. Baras, Effects of planetary ball milling on AlCoCrFeNi high entropy alloys prepared by spark plasma sintering: experiments and molecular dynamics study, *J Alloys Compd.* 820 (2020).
- [30] D.Q. Doan, T.H. Fang, T.H. Chen, Influences of grain size and temperature on tribological characteristics of CuAlNi alloys under nanoindentation and nanoscratch, *Int. J. Mech. Sci.* 185 (2020) 19.
- [31] J.W. Choi, J.T. Kim, S.H. Hong, et al., Investigation of correlation between the microstructural characteristics and mechanical properties of (CoCuFeNi)100-xAlx high entropy alloys, *J Alloys Compd.* 933 (2023), 167679.
- [32] M.J. Kim, G.C. Kang, S.H. Hong, et al., Understanding microstructure and mechanical properties of (AlTa(0.76))xCoCrFeNi(2.1) eutectic high entropy alloys via thermo-physical parameters, *J Mater Sci Technol.* 54 (22) (2020) 7.
- [33] L.Q. Cui, C.H. Yu, S. Jiang, Mechanical and tribological performance of AlCr0.5NbTaxTi4-x (x = 0, 0.5, 1) refractory high-entropy alloys, *Journal of Materials Science & Technology*. 96 (2022) 10.
- [34] M.J. Kim, J.T. Kim, J. Elyorjon, et al., Understanding the microstructure and mechanical properties of Ta Al0.7CoCrFeNi2.1 eutectic high entropy composites: Multi-scale deformation mechanism analysis, *Compos. B. Eng.* 214 (5) (2021), 108750.
- [35] J.W. Choi, J.T. Kim, S.H. Hong, et al., Analysis of phase transformation and deformation behaviors on Laves phase of as-cast (CoCuFeNi)100-xZrx high entropy alloys, *J Alloys Compund.* (2022).
- [36] Y.F. Shen, L. Lu, Q.H. Lu, Z.H. Jin, K. Lu, Tensile properties of copper with nanoscale twins, *Scr. Mater.* 52 (2005) 989.
- [37] H. Gu, C. Liu, F. Yuan, F. Han, Y. Zhang, M. Ali, W. Guo, J. Ren, L. Zhang, S. Wu, G. Li, Deformation twinning in octahedron-based face-centered cubic metallic structures: Localized shear-force dipoles drive atomic displacements, *J. Mater. Sci. Technol.* 126 (2022) 116–126.
- [38] I. Shabib, R.E. Miller, Deformation characteristics and stress-strain response of nanotwinned copper via molecular dynamics simulation, *Acta Mater.* 57 (2009) 4364–4373.
- [39] G. Laplanche, A. Kostka, O.M. Horst, G. Eggeler, E.P. George, Microstructure evolution and critical stress for twinning in the CrMnFeCoNi high-entropy alloy, *Acta Mater.* 118 (2016) 152–163.
- [40] B. Kang, T. Kong, H.J. Ryu, S.H. Hong, Superior mechanical properties and strengthening mechanisms of lightweight AlxCrNbVMo refractory high-entropy alloys (x = 0, 0.5, 1.0) fabricated by the powder metallurgy process, *J. Mater. Sci. Technol.* 69 (2021) 32–41.